Volume 1
Number 3
1 May 2024
Pages 331–614

RSC Applied Interfaces

rsc.li/RSCApplInter

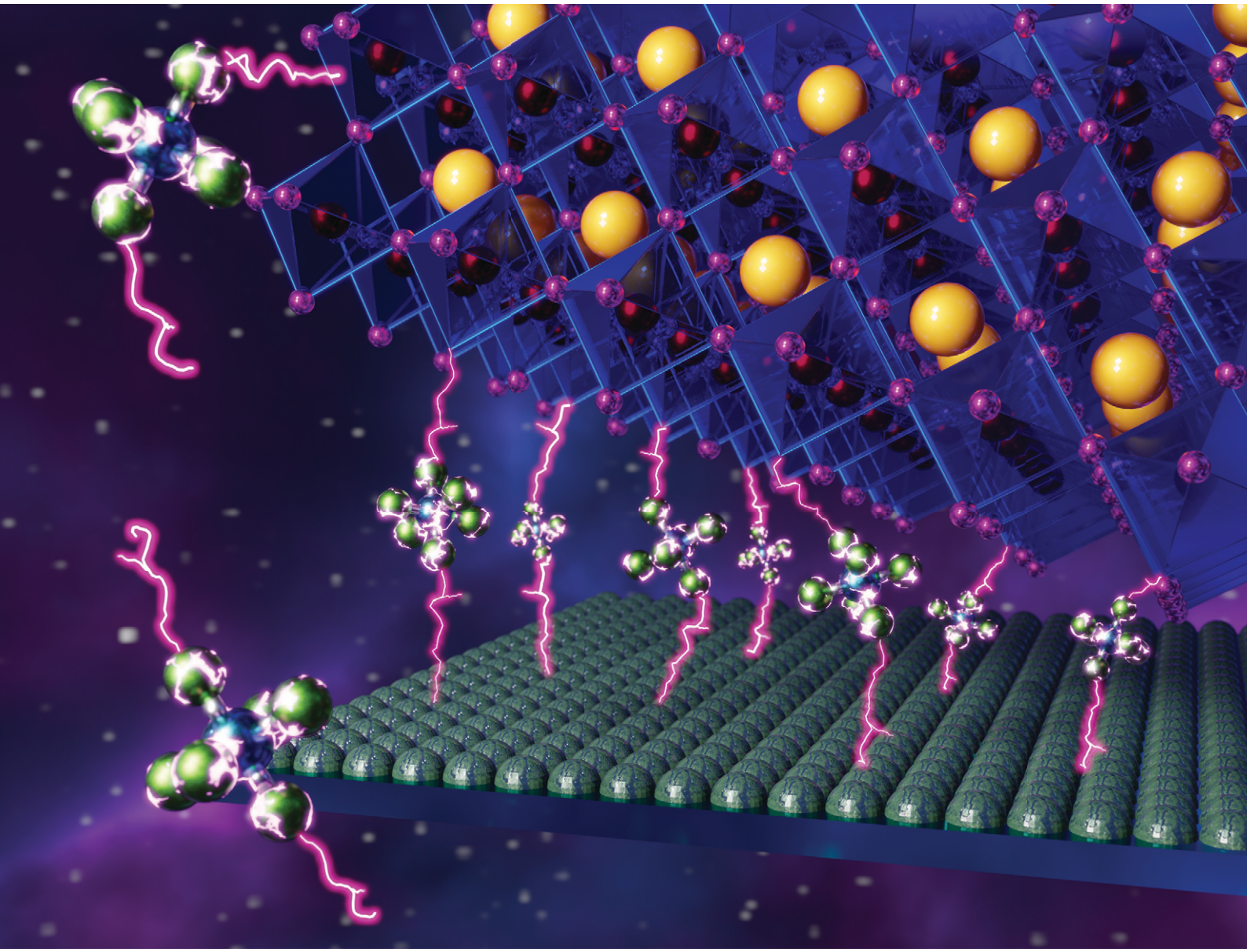

ISSN 2755-3701

ROYAL SOCIETY OF CHEMISTRY

PAPER

Zong-Xuan She and Sheng-Hsiung Yang
Interfacial modification between NiO_x and perovskite layers with hexafluorophosphate salts for enhancing device efficiency and stability of perovskite solar cells

RSC Applied Interfaces

ROYAL SOCIETY OF CHEMISTRY

PAPER

View Article Online
View Journal | View Issue

Cite this: *RSC Appl. Interfaces*, 2024, 1, 443

Interfacial modification between NiO_x and perovskite layers with hexafluorophosphate salts for enhancing device efficiency and stability of perovskite solar cells†

Zong-Xuan She and Sheng-Hsiung Yang *

Received 20th December 2023,
Accepted 4th March 2024

DOI: 10.1039/d3lf00258f

rsc.li/RSCApplInter

Inorganic metal oxides like nickel oxides (NiO_x) have been largely adopted as hole transport layers (HTLs) for the fabrication of perovskite solar cells (PSCs). Reducing interfacial defects between the NiO_x HTL and the perovskite absorbing layer is always a key issue in achieving high efficiency and long-term stability of PSCs. In this work, we first utilized inorganic hexafluorophosphate salts including NH_4PF_6, $LiPF_6$, and $NaPF_6$ to modify the surface of NiO_x through interactions between Ni atoms and PF_6^- groups. The incorporation of those salts not only decreased the defects at the NiO_x/perovskite interface but also optimized the energy levels of NiO_x to match with the perovskite. After the surface passivation of NiO_x, the up-lying perovskite consequently exhibited larger grain sizes and shorter carrier lifetime. The PSC based on an NH_4PF_6-modified NiO_x HTL showed the best efficiency of 17.28% and a long device lifetime of over 108 days, which was significantly better than the controlled device using the pristine NiO_x layer. Our experimental results demonstrate that interface modification of NiO_x by hexafluorophosphate salts is an effective strategy to optimize the performance of PSCs.

1. Introduction

Perovskites have garnered substantial research interest for photovoltaic applications owing to their high visible light absorption, long carrier diffusion length, high carrier mobility, low exciton binding energy, and tunable bandgap.[1–4] In recent years, the development of perovskite solar cells (PSCs) in laboratories has been rapidly boosted with the best efficiency of 26.1%.[5] The chemical formula of perovskite materials is ABX_3, where A can be an organic/inorganic monovalent cation, B is a divalent metal cation, and X is a halide anion. Monocationic perovskites have been extensively utilized as active layers in PSCs, like methylammonium lead iodide ($MAPbI_3$), formamidinium lead iodide ($FAPbI_3$), and cesium lead iodide ($CsPbI_3$).[6–8] However, monocationic perovskites are considered to exhibit low thermal and moisture stability, which hinders their applicability to PSCs. To improve the stability and efficiency of PSCs, the mainstream approach adopts mixed cation perovskites as active layers.[9] Li *et al.* utilized a mixed cation perovskite $FA_{1-x}MA_xPbI_3$ with a FA^+:MA^+ molar ratio of 0.7:0.3 as a light absorber.[10] The best device achieved a maximum power conversion efficiency (PCE) of 16%, an open-circuit voltage (V_{OC}) of 1.03 V, a short-circuit current density (J_{SC}) of 22.6 mA cm^{-2}, and a fill factor (FF) of 0.68. Furthermore, the unsealed device retained its performance without any PCE loss for 20 days in an ambient environment. Bolink and his coworkers demonstrated a triple-cation $Cs_{0.5}FA_{0.4}MA_{0.1}Pb(I_{0.83}Br_{0.17})_3$ perovskite film by simultaneous thermal vacuum deposition.[11] The optical absorption of the triple-cation perovskite layer was unaltered for days during continuous exposure to air at 25 °C and 40% relative humidity (RH) condition. The optimized PSC showed the best PCE of 16% with negligible hysteresis and an external quantum efficiency (EQE) of 70–85% in the whole visible light range. It is undeniable that using multi-cation perovskite materials is one of the key factors to enhance the efficiency and stability of PSCs.

PSCs with a p–i–n configuration offer various advantages including straightforward fabrication, optimal energy level alignment, little hysteresis effect, and long-term stability.[12–16] Choosing suitable hole transport materials is critical for enabling efficient hole extraction and suppressing detrimental electron recombination. Common hole transport layers (HTLs) for PSCs include inorganic metal oxides (such

Institute of Lighting and Energy Photonics, College of Photonics, National Yang Ming Chiao Tung University, No. 301, Section 2, Gaofa 3rd Road, Guiren District, Tainan 711010, Taiwan, Republic of China. E-mail: yangsh@nycu.edu.tw

† Electronic supplementary information (ESI) available. See DOI: https://doi.org/10.1039/d3lf00258f

as NiO_x and CuO_x) and conductive polymers (like P3HT, PTAA, and PEDOT:PSS).[17,18] The high price, low hole mobility, and unsuitable energy level alignments of organic polymers limit the development of PSCs using organic HTLs.[19–21] In comparison, inorganic oxides have several benefits for fabricating efficient and stable PSCs, including optimal band alignment with perovskites, low resistivity, environmental stability, and cost-effectiveness.[22] Among inorganic HTLs, NiO_x is extensively utilized because of easy processing, low cost, high transmittance in the visible range, and facile preparation of precursor solutions. However, direct contact between NiO_x and perovskites usually generates issues that reduce the efficiency and stability of PSCs. In accordance with prior research reports,[23,24] Ni^{3+} on the NiO_x surface is predisposed to interfacial redox reactions with A-site cations of the perovskite, consuming the ratio of Ni^{3+} in NiO_x, thereby decreasing intrinsic conductivity and increasing charge recombination. In addition, this accelerates the deprotonation of the organic ammonium group to amine precursor and perovskite degradation to induce severe instability of devices.

To manufacture highly efficient and stable PSCs, addressing surface defects in NiO_x is crucial. Here, we demonstrate that inorganic hexafluorophosphate salts, like NH_4PF_6, $LiPF_6$ and $NaPF_6$, can effectively passivate surface defects of NiO_x and significantly improve device performance. The device architecture of our PSCs is depicted in Fig. 1. In this work, the NiO_x/perovskite interfacial contact was modified by introducing an ultrathin layer of NH_4PF_6, $LiPF_6$, or $NaPF_6$ to prevent direct contact between NiO_x and perovskites, as shown in Fig. 1. The PF_6^- groups can interact with Ni atoms to tightly attach to the NiO_x layer. The salt modification can effectively enhance the carrier extraction capability of NiO_x owing to reduced defects and favorable energy level alignment. The experimental results reveal that the NH_4PF_6, $LiPF_6$, and $NaPF_6$-modified NiO_x devices exhibited the best PCE of 17.28%, 14.87%, and 14.88%, respectively, relative to the controlled device with a PCE of 13.98%. Moreover, the modified devices showed preferable steady-state PCE output and much longer device lifetime up to 108 days.

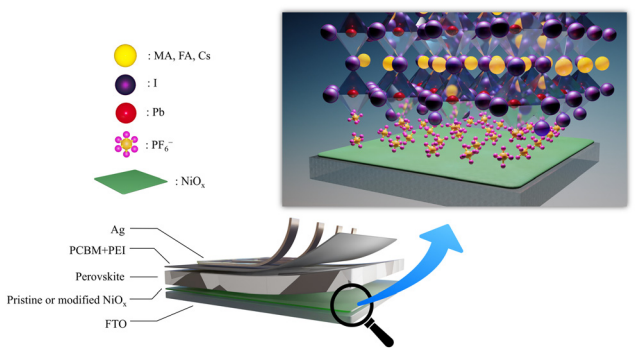

Fig. 1 Device architecture of PSCs with the enlarged illustration of the salt-modified NiO_x/perovskite interface.

2. Experimental section

2.1 Materials

The patterned fluorine-doped tin oxide (FTO, 7 Ω per square)-coated glass substrates were bought from LiveStrong Optoelectronics Technology Co., Ltd. Nickel acetate tetrahydrate ($Ni(OAc)_2{\cdot}4H_2O$, purity 98+%), lead bromide ($PbBr_2$, purity 98+%), lead iodide (PbI_2, purity 99.9985%), and cesium iodide (CsI, purity 99.9%) were purchased from Alfa Aesar. Methylammonium bromide (MABr, purity 98.0%) and formamidinium iodide (FAI, purity 98%) were bought from TCI and Greatcell Solar Materials Pty Ltd., respectively. Ethanolamine (purity 99%) and tetra-*n*-butylammonium tetrafluoroborate ($TBABF_4$, purity 98%) were purchased from Acros. [6,6]-Phenyl-C_{61}-butyric acid methyl ester ($PC_{61}BM$, purity 99%) was bought from Solenne B. V. Polyethyleneimine (PEI, molecular weight 25 000 g mol^{-1}) was bought from Sigma-Aldrich. Three hexafluorophosphate salts, including lithium hexafluorophosphate ($LiPF_6$, purity 98%), sodium hexafluorophosphate ($NaPF_6$, purity 98%), and ammonium hexafluorophosphate (NH_4PF_6, purity 99%), were purchased from Thermo Fisher Scientific, Matrix Scientific, and Sigma-Aldrich, respectively. Other solvents were purchased from Alfa Aesar or Acros and used without further purification.

2.2 Preparation of NiO_x layers

$Ni(OAc)_2{\cdot}4H_2O$ (0.124 g, 0.5 mmol) and 30 μL of ethanolamine were dissolved in 5 mL of isopropanol (IPA). The solution was heated and stirred at 70 °C for 24 h to form a translucent green precursor solution. The precursor solution was then spin-coated onto the FTO substrate at a speed of 1500 rpm for 30 s. The substrate was dried at 75 °C for 10 min and then calcined in a high-temperature oven at 450 °C for 1 h to obtain the pristine NiO_x layer. To prepare the modified NiO_x films, NH_4PF_6 (0.6 mg mL^{-1} in acetonitrile), $NaPF_6$ (0.6 mg mL^{-1} in methanol), or $LiPF_6$ (0.6 mg mL^{-1} in methanol) was individually spin-coated on different NiO_x from their solutions at 1000 rpm for 30 s and dried at 80 °C for 10 min.

2.3 Device fabrication

The device structure in this study is FTO/pristine or modified NiO_x/perovskite/PCBM + $TBABF_4$/PEI/Ag. The FTO substrates were sequentially sonicated in detergent, deionized water, acetone, and IPA for 20 min, followed by oxygen plasma treatment for 15 min. The pristine or modified NiO_x layers as the HTLs were prepared on the FTO substrates according to section 2.2. The perovskite layer was then deposited on top of the NiO_x HTL, followed by the deposition of the PCBM + $TBABF_4$ layer as the electron transport layer (ETL). The details for the preparation and deposition of the perovskite and PCBM + $TBABF_4$ layers were referred to our previous report.[25] Afterward, 0.1 mol% PEI in anhydrous IPA was spin-coated onto the PCBM layer at 4500 rpm for 30 s. Finally, 100 nm-thick Ag electrodes were thermally evaporated under a base

pressure of 8×10^{-6} torr. The active area of each device is 4.5 mm^2.

2.4 Characterization

The current density–voltage (*J–V*) characteristics of PSCs were recorded using a Keithley 2400 source meter under simulated AM 1.5G solar irradiation (1000 W xenon short arc lamp, Yamashita Denso YSS-100A). The dark current measurement of PSCs was performed using the same source meter in the dark environment. EQE and integrated current density data were measured using a self-assembled system consisting of a Keithley 2400 source meter, an ABET Technologies LS 150 xenon lamp, and a Prince Instruments Acton 2150 monochromator. To investigate the stability of the devices, the encapsulated PSCs were stored in a humidity control box

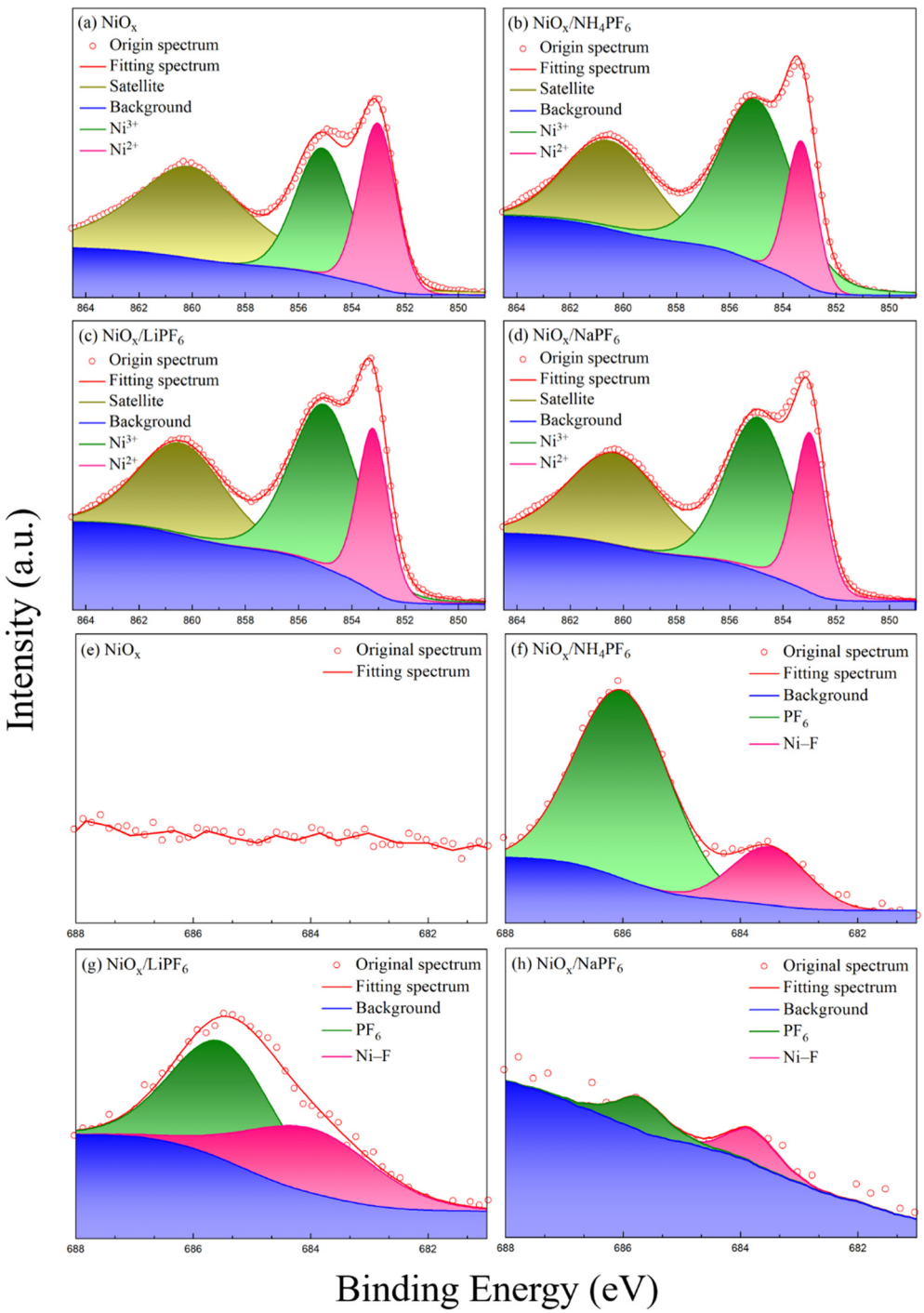

Fig. 2 XPS spectra of (a–d) Ni 2p and (e–h) F 1s elements in the pristine and modified NiO_x films.

at room temperature with 40% RH and their device performance was acquired at certain intervals. The presence of NH_4PF_6, $LiPF_6$, and $NaPF_6$ in the samples was analyzed by X-ray photoelectron spectroscopy (XPS) using a Thermo Scientific K-Alpha spectrometer. The surface topography and surface roughness of the pristine and modified NiO_x thin films were measured using a Bruker Innova atomic force microscope (AFM). Ultraviolet photoelectron spectroscopy (UPS) measurements of the pristine and modified NiO_x thin films were performed using a Thermo VG-Scientific/Sigma Probe spectrometer, with a He I ($h\nu$ = 21.22 eV) discharge lamp as the excitation source. An ultrahigh-resolution ZEISS Crossbeam scanning electron microscope (SEM) was utilized to examine the surface morphologies of the samples. A Rigaku D/MAX2500 X-ray diffractometer was employed to obtain the X-ray diffraction (XRD) patterns of the samples, which were then analyzed to determine their lattice type and crystallinity. Steady-state photoluminescence (PL) of the perovskite films was measured using an Oxford Instruments ANDOR Kymera 193i-B1 spectrometer. An Omicron QuixX 473-100 PS laser with a wavelength of 473 nm was used as the excitation light source. For time-resolved PL (TR-PL) decay measurements, a time-correlated single photon counting module (PicoQuant MultiHarp 150 4N) and a photomultiplier tube through an Andor Kymera 328i spectrometer were used to collect TR-PL decay signals. A 473 nm pulsed laser (Omicron) was used as the excitation light source.

3. Results and discussion

3.1 Analysis of NiO_x films

To confirm the presence of NH_4PF_6 (or $LiPF_6$, $NaPF_6$) and understand the interaction between NiO_x and the three modifiers, XPS measurements of the pristine and modified NiO_x films were carried out, as shown in Fig. 2. The Ni $2p_{3/2}$ spectra consist of two characteristic peaks from Ni^{2+} and Ni^{3+} species at 855 and 853 eV, respectively. It is reported that the higher Ni^{3+}/Ni^{2+} area ratio means better conductivity of NiO_x.[26] From Fig. 2a–d, the Ni^{3+}/Ni^{2+} ratio of the pristine NiO_x and NH_4PF_6, $LiPF_6$, and $NaPF_6$-modified NiO_x films are calculated to be 1.22, 2.94, 2.45, and 2.38, respectively. The Ni^{3+}/Ni^{2+} ratio is significantly higher for the modified NiO_x films compared to the pristine one, especially the NH_4PF_6-modified NiO_x. Due to the introduction of hexafluorophosphate salts, the cations on those salts occupied the original Ni^{2+} sites on the NiO_x surface. The neighboring Ni^{2+} would convert to Ni^{3+} to maintain the electroneutrality of the material, causing the Ni^{3+} concentration in NiO_x to increase. Obviously, the conductivity as well as the hole transport properties of NiO_x can be improved by introducing those hexafluorophosphate salts. Interestingly, different oxidation states of Ni^{2+} and Ni^{3+} ions of non-stoichiometric NiO_x may show different effects on device performance. Choy and his coworkers reported that the additional Ni^{3+} state has a detrimental impact on the electrical properties of NiO_x and thus decreases the device performance of organic solar cells.[27] The F 1s spectra in Fig. 2f–h reveal the existence of NH_4PF_6, $LiPF_6$, or $NaPF_6$ in the modified NiO_x films. In contrast, no F 1s signal is found in Fig. 2e for the pristine NiO_x. The peak at around 686 eV in Fig. 2f–h is attributed to the F atom from PF_6^- groups,[28,29] while the peak at around 684 eV corresponds to the interaction between F and Ni atoms.[30,31] Besides, the N 1s, P 2p, Na 1s, and Li 1s signals from the modified NiO_x films are clearly observed at 399.4, 113, 1071, and 55.53 eV, respectively, in Fig. S1 in the ESI.† The XPS results suggest that the incorporation of NH_4PF_6, $LiPF_6$, and $NaPF_6$ can effectively enhance the overall carrier transport ability of the NiO_x film, implying the passivation of surface defects on NiO_x.

The surface morphology of the pristine and modified NiO_x films was investigated by AFM. As shown in Fig. S2,† the average roughness (R_a) of the pristine NiO_x and NH_4PF_6, $LiPF_6$, and $NaPF_6$-modified NiO_x films was determined to be 16.8, 14.3, 14.5, and 15.3 nm, respectively. The reduction in the surface roughness of the NiO_x films can be attributed to the ability of PF_6^- groups to effectively passivate NiO_x surface defects *via* Ni–F interactions. Incorporating NH_4PF_6, $LiPF_6$, or $NaPF_6$ to obtain smoothened NiO_x is advantageous for subsequent deposition of perovskite films. The top-view SEM images of the pristine and modified NiO_x films are provided in Fig. S3.† The size and distribution of NiO_x grains look similar for all samples. It is difficult to tell how those NiO_x morphologies may affect the formation of perovskites. On the other hand, we realize that salt-modified NiO_x has lower surface roughness from AFM experiments, which is helpful for better perovskite growth. To elucidate the impact of surface modification on the energy levels of NiO_x, UPS measurements were conducted on the pristine NiO_x and NH_4PF_6, $LiPF_6$, and $NaPF_6$-modified NiO_x films. From the UPS spectra in Fig. 3a and b, the Fermi level (E_F) of the pristine NiO_x and NH_4PF_6, $LiPF_6$, and $NaPF_6$-modified NiO_x films were calculated to be −4.09, −3.95, −3.89, and −3.88 eV, respectively, by subtracting the energy cutoff in the high binding energy region (about 17.3 eV) from the excitation photon energy (21.22 eV).[32] The valence band (VB) was then deduced from the low energy cutoff value (about 1 eV) to be −5.14, −5.4, −5.39, and −5.3 eV, respectively, for the original NiO_x and NH_4PF_6, $LiPF_6$, and $NaPF_6$-modified NiO_x films. The VB values obtained for the NiO_x films in this work are comparable to previously reported values for NiO_x in the literature.[33,34] Therefore, the energy level diagram of the whole device is constructed and displayed in Fig. 3c. The surface modification using the three PF_6-containing salts can effectively downshift the energy levels of the NiO_x film, optimizing the band alignment and reducing the energy barrier between NiO_x and the perovskite layer. Considering the CB of NiO_x-based HTLs is sufficiently high (from −1.8 to −2.23 eV), NiO_x is able to efficiently prevent electron leakage.[35,36] The CB of our salt-modified NiO_x is even higher from −1.55 to −1.63 eV, exhibiting outstanding electron

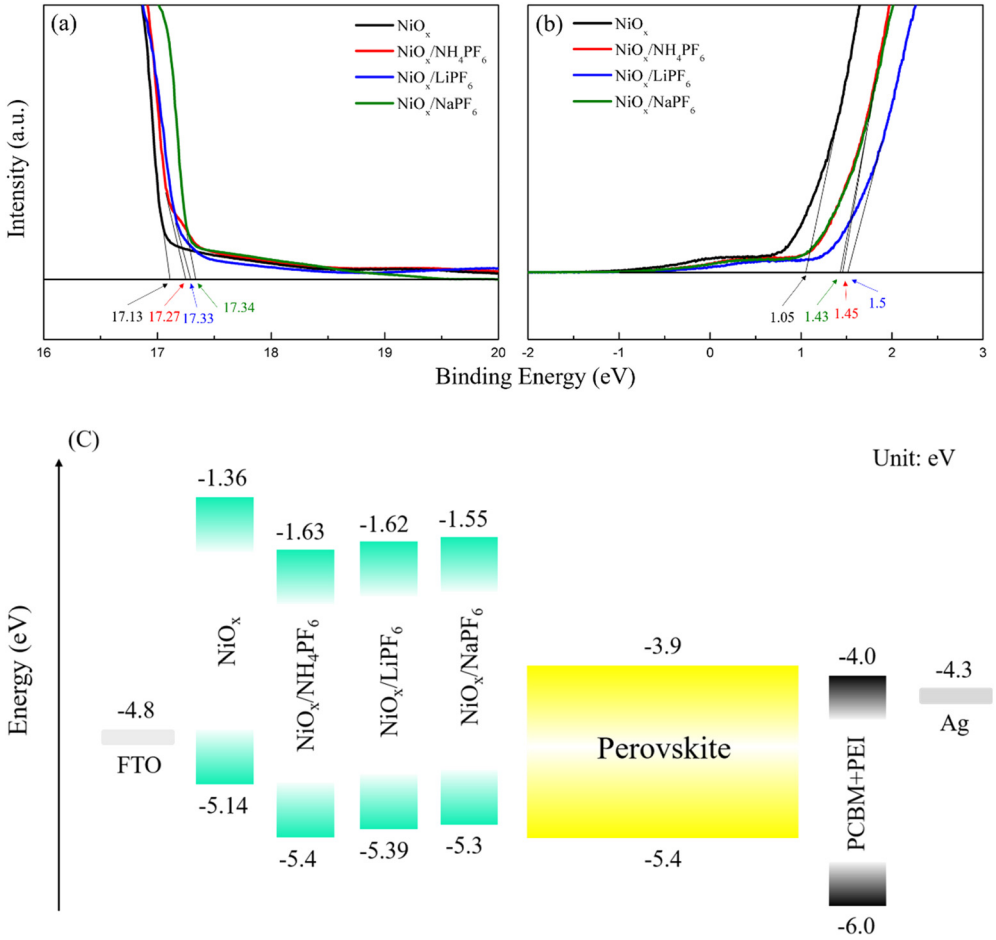

Fig. 3 UPS spectra of the pristine and modified NiO_x films in the (a) low and (b) high binding energy regions; (c) energy level diagram of PSCs.

blocking behaviors. As mentioned in the XPS analysis, the incorporation of hexafluorophosphate salts makes NiO_x exhibit more p-type properties with higher hole concentration, and therefore the VB level of the modified NiO_x shows a downward shift. Among the three salt-modified NiO_x, we speculate that the difference in energy levels originates from different types and ionic sizes of the three cations (NH_4^+, Li^+, and Na^+). In particular, NH_4^+ has the largest ionic size that is suitable for occupying Ni^{2+} sites and modifying energy levels of NiO_x.

3.2 Characterization of perovskites on different NiO_x films

It is understandable that a smooth defect-free NiO_x surface is favorable for the formation of high-quality perovskite layers with larger grain sizes and fewer boundaries. The SEM images of the perovskite films deposited on the pristine and modified NiO_x are displayed in Fig. 4, revealing discernible differences in perovskite morphology and grain size. Compared to perovskites on the pristine NiO_x, the perovskite films deposited on the salt-modified NiO_x exhibit markedly larger grain sizes, indicating that the interface modification facilitates favorable perovskite crystallization and grain growth. As for the SEM images in Fig. 4b–d, the morphological difference of the perovskite comes from NiO_x underlayers with different surface properties which were modified by various salts carrying different cations. Among them, NH_4PF_6-modified NiO_x has the lowest roughness, causing the largest perovskite grain size (average 566.7 nm). The large grain size of perovskites with fewer boundaries can effectively reduce charge recombination, thereby enhancing the extraction and transport of carriers. In addition to SEM observation, XRD analysis was also performed to provide the crystallinity of perovskite films deposited on the different NiO_x layers. In Fig. S4,† several intense diffraction peaks at 2θ = 14.2°, 19.9°, 24.5°, 28.3°, 31.8°, 35°, 40.5°, and 43.1° were observed, corresponding to the (001), (011), (111), (002), (012), (112), (022), and (003) planes of the cubic perovskite phase, respectively, which are consistent with the previous reports.[32] Additionally, the perovskite films deposited on the salt-modified NiO_x exhibit more intense diffraction peaks, indicating that salt incorporation promotes the growth of perovskite grains with higher crystallinity.

The PL spectra in Fig. 5a demonstrate that the perovskites grown on the salt-modified NiO_x films exhibit lower PL intensity compared to that on the pristine NiO_x. The results suggest that interface modification enhances the carrier extraction of the NiO_x HTL and suppresses charge

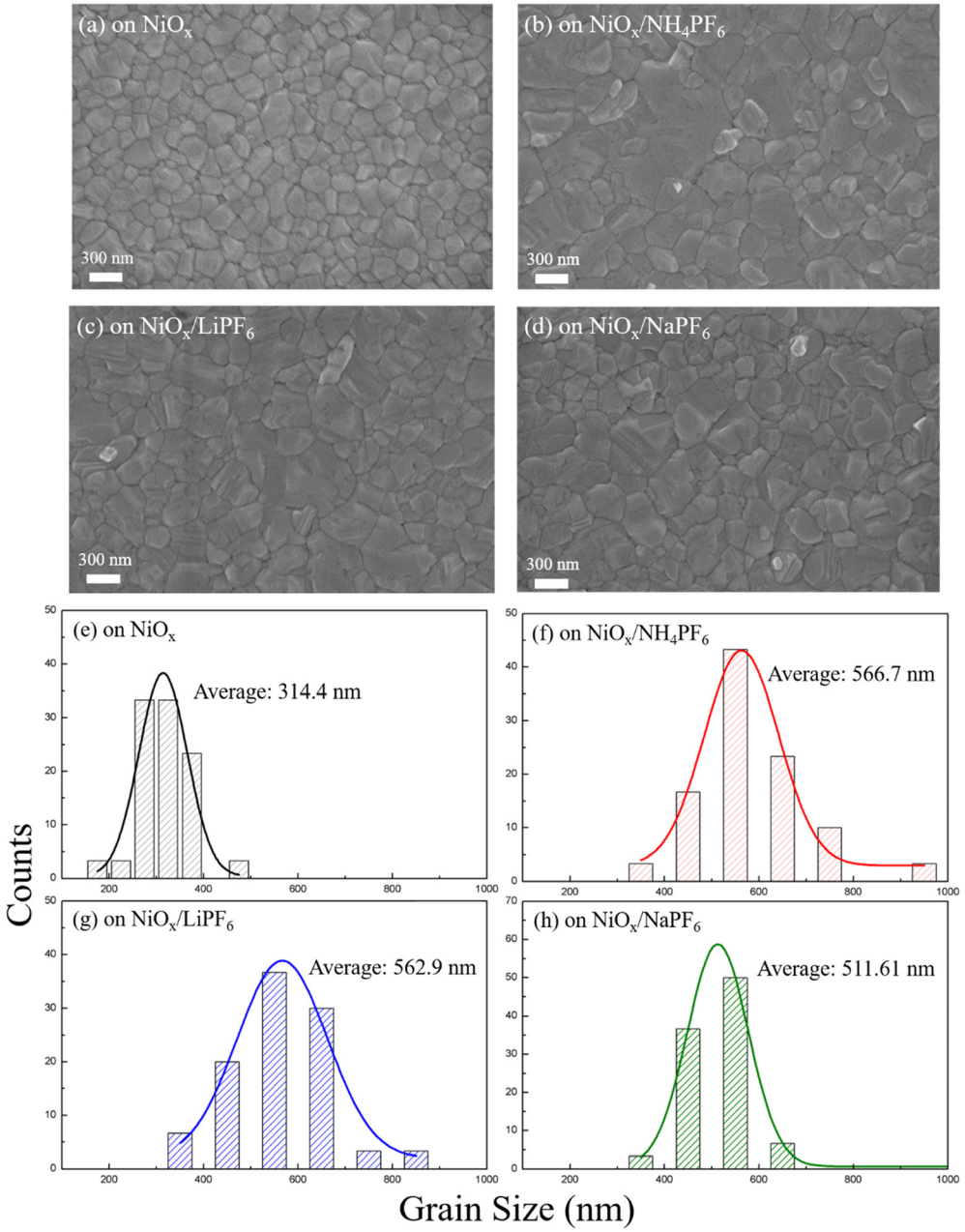

Fig. 4 (a–d) Top-view SEM images and (e–h) grain size distribution of perovskite films on the pristine or modified NiO_x layers.

recombination. Among the three salts, NH_4PF_6 modification induces the most pronounced decrease in PL intensity, indicating its effective passivation capability to bring improvements in J_{SC} and FF of PSCs. To further corroborate the phenomenon of PL attenuation, TR-PL decay measurements of the perovskite films deposited on the various NiO_x layers were carried out and the corresponding decay curves are displayed in Fig. 5b. The fast-decay constant τ_1, slow-decay constant τ_2, and average carrier lifetime τ_{avg} from the bi-exponential fitting of PL decay curves are listed in Table S1.† The perovskites on the pristine NiO_x and NH_4PF_6, $LiPF_6$, and $NaPF_6$-modified NiO_x have a τ_{avg} of 230.8, 88.3, 144, and 185.1 ns, respectively. The reduced τ_{avg} can be attributed to the enhanced carrier extraction ability of NiO_x to reduce the PL emission of the perovskites. Apparently, the TR-PL decay results are in agreement with the downtrend of PL intensity. The change in TR-PL decay curves and carrier lifetime can be realized by interface modification of NiO_x using the three hexafluorophosphate salts with different cations, as discussed in the previous UPS analysis and SEM observation of perovskites. We notice that NH_4PF_6 incorporation leads to the shortest carrier lifetime of perovskites and therefore, the best PSC performance based on the NH_4PF_6-modified NiO_x HTL is expected. To summarize, the passivation of surface defects by salt insertion between NiO_x and perovskite layers brought about

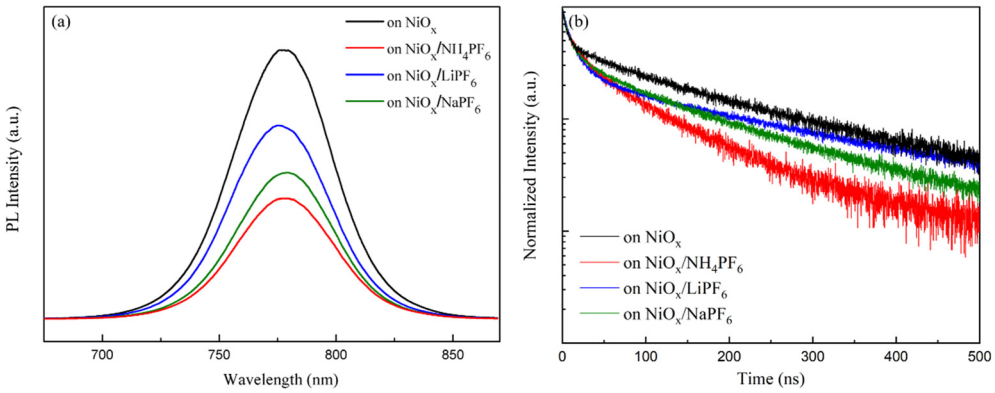

Fig. 5 (a) PL emission spectra and (b) TR-PL decay curves of the perovskites on the pristine NiO_x and NH_4PF_6, $LiPF_6$, and $NaPF_6$-modified NiO_x films.

improved conductivity, lowered surface roughness, and enhanced carrier extraction ability of NiO_x. Meanwhile, larger perovskite grains as well as matched energy levels at the NiO_x/perovskite interface were acquired.

3.3 Electrical and stability measurements of PSCs

The device architecture in this study is FTO/pristine or modified NiO_x/perovskite/PCBM + $TBABF_4$/PEI/Ag, where NH_4PF_6, $LiPF_6$, or $NaPF_6$ is solely inserted between NiO_x and the perovskite layer as the modifier. It is important to reduce the redox reaction at the NiO_x/perovskite interface to improve the device efficiency and stability. Two small molecules, 4-(2-aminoethyl)benzoic acid bromide and potassium thiocyanate, were proposed to be inserted between the NiO_x HTL and perovskite film to diminish the redox reaction between the two layers in the literature.[37,38] In this study, hexafluorophosphate salts were selected to deposit on top of NiO_x to prevent direct contact between NiO_x and the perovskite surface, thus delaying the degradation of perovskite films. To evaluate the influences of interfacial defects and density of trap states on charge transport within devices, dark currents of PSCs with the pristine and modified NiO_x HTLs were measured, as shown in Fig. S5.† Under the reverse bias from −1 to 0 V, PSCs with NH_4PF_6 and $LiPF_6$-modified NiO_x HTLs exhibited lower leakage current density compared with the pristine NiO_x device, meaning that charge extraction was facilitated and recombination was mitigated through interface modification. Specifically, NH_4PF_6 possesses the most significant passivation ability among the

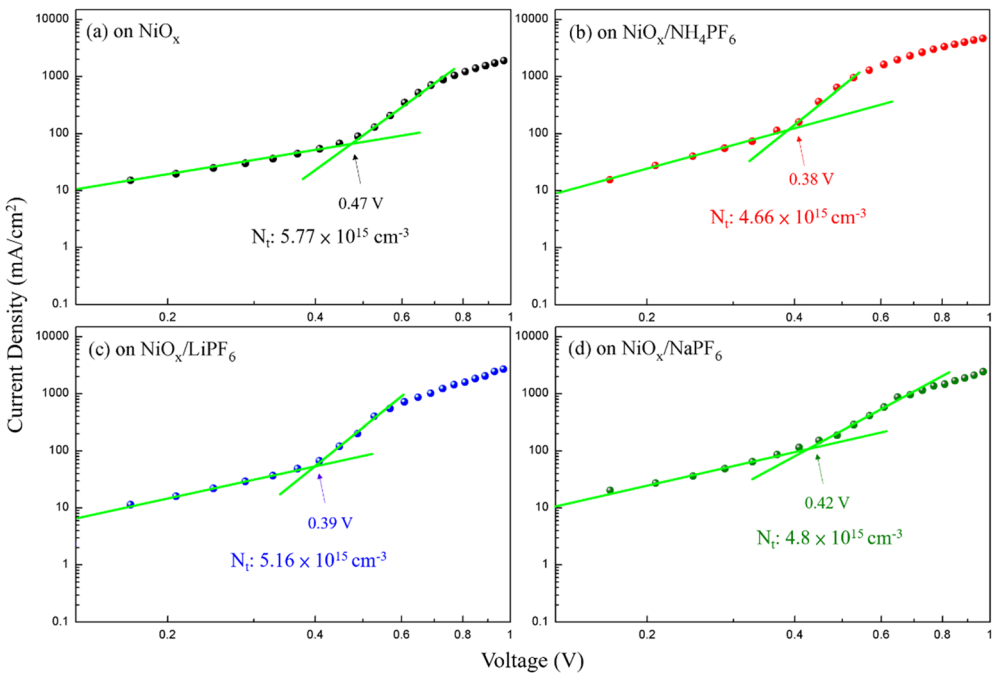

Fig. 6 Dark *J*–*V* characteristics of PSCs based on the (a) pristine NiO_x and (b) NH_4PF_6-, (c) $LiPF_6$-, and (d) $NaPF_6$-modified NiO_x with the SCLC analysis.

three salts to promote the device performance. The defect densities (N_t) were calculated *via* the space-charge-limited current (SCLC) analysis,[39,40] as depicted in Fig. 6. The N_t values of the devices were computed by eqn (1):

$$N_t = \frac{2\varepsilon_0\varepsilon_r V_{TFL}}{qL^2} \quad (1)$$

where V_{TFL}, ε_0, ε_r, q, and L represent the trap-filled limit voltage, vacuum permittivity, relative dielectric constant of the perovskite $Cs_{0.05}FA_{0.81}MA_{0.14}Pb(Br_{0.15}I_{0.85})_3$,[41] elementary charge, and the thickness of the perovskite film. Through the salt modification of the NiO_x films, the V_{TFL} was determined to be 0.47, 0.38, 0.39, and 0.42 V for the pristine NiO_x and NH_4PF_6, $LiPF_6$, and $NaPF_6$-modified NiO_x PSCs, respectively. Moreover, the N_t value was reduced from 5.77×10^{15} cm^{-3} for the pristine NiO_x device to 4.66×10^{15}, 5.16×10^{15}, and 4.8×10^{15} cm^{-3} for the NH_4PF_6, $LiPF_6$, and $NaPF_6$-modified NiO_x PSCs, respectively. The results demonstrate that salt modification effectively passivated the interfacial defects between NiO_x and the perovskite. The photovoltaic performance of the devices was assessed under AM 1.5G illumination at 100 mW cm^{-2} and the *J–V* characteristics of the PSCs are displayed in Fig. 7a. The controlled device based on the pristine NiO_x HTL had the best PCE of 13.98% and average J_{SC} of 20.46 mA cm^{-2}, V_{OC} of 0.97 V, FF of 65.39%, and PCE of 12.94% from 30 devices. The champion PSC was achieved by incorporating the NH_4PF_6-modified NiO_x film with a maximum PCE of 17.28% and average J_{SC} of 21.86 mA cm^{-2}, V_{OC} of 1.01 V, FF of 70.97%, and PCE of 15.62%. The enhanced performance can be attributed to the passivation of interfacial defects, high-quality perovskite crystals, and favorable energy level alignment between NiO_x and the perovskite by introducing NH_4PF_6 as the surface modifier. Besides, the device using the $LiPF_6$-modified NiO_x film as the HTL exhibited a maximum PCE of 14.87% and average J_{SC} of 20.99 mA cm^{-2}, V_{OC} of 0.97 V, FF of 68.54%, and PCE of 14.03%. By using the $NaPF_6$-modified NiO_x HTL, the device exhibited a maximum PCE of 14.88% and average J_{SC} of 20.73 mA cm^{-2}, V_{OC} of 0.99 V, FF of 69.3%, and PCE of 14.26%, which was still better than the controlled device. Table 1 presents the best PCE and average photovoltaic parameters from 30 devices incorporating the pristine or salt-modified NiO_x HTL. The performance of our devices is not very good as compared to those of reported NiO_x-based perovskite solar cells with a PCE of 18.75–20.13% or a long device lifetime over 3000 h,[42,43] mainly due to different processing equipment and environments. Limited by our processing facilities, the devices were not manufactured under low water/oxygen conditions throughout the entire process. Besides, the electrical measurements of our devices were carried out in an ambient environment. The above factors may affect the performance of PSCs. Fig. 7b displays the integrated current density curves and EQE spectra of PSCs using the pristine and salt-modified NiO_x HTLs from 300 to 830 nm. The results demonstrate the substantially enhanced EQE values for the devices incorporating salt-modified NiO_x compared to the pristine one, with NH_4PF_6 modification exhibiting the most pronounced improvement. The integrated current density was acquired to be 19.12, 20.7, 20.3, and 19.6 mA cm^{-2} for the pristine NiO_x and NH_4PF_6, $LiPF_6$, and $NaPF_6$-modified NiO_x devices, respectively, which coordinated well with the measured J_{SC} values.

Light intensity dependent J_{SC} and V_{OC} measurements were conducted to elucidate the interfacial carrier recombination process. The correlation between J_{SC} and illumination intensity is shown in Fig. 8a, which follows a power law relation: $J_{SC} \propto I^{\alpha}$, where I is the light intensity and α is the exponential factor.[44] The α of the PSCs with salt-modified NiO_x HTLs (~0.995) is closer to 1 that is higher than the controlled device (α = 0.94), meaning that the J_{SC} of the salt-modified devices is approximately proportional to the incident light intensity and the recombination is inhibited.[45] Fig. 8b depicts the relationship between V_{OC} and light intensity, revealing that the slope of the three salt-modified NiO_x devices is higher than that of the controlled one. According to the previous literature,[46,47] the relationship between V_{OC} and light intensity can be described by eqn (2):

$$V_{oc} = \left(\frac{nKT}{q}\right)\ln\left(\frac{J_{sc}}{J_0} + 1\right) \quad (2)$$

where n is the ideality factor, K is Boltzmann's constant, T is the absolute temperature, q is the elementary charge, J_{SC} is

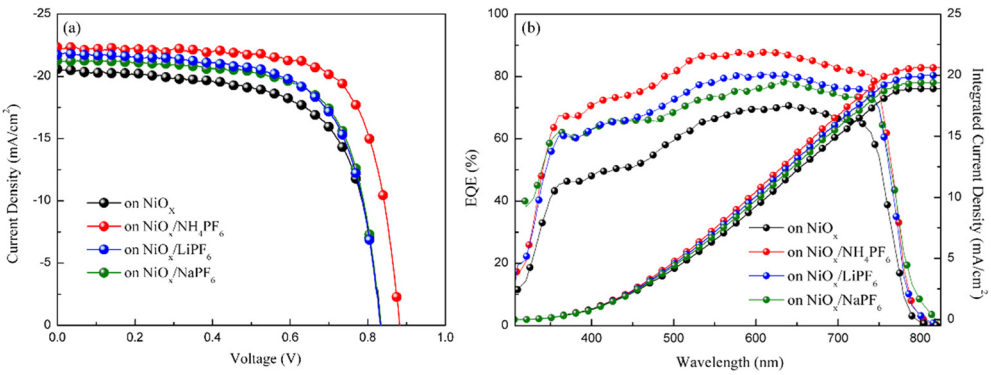

Fig. 7 (a) *J–V* characteristics and (b) EQE spectra and integrated current density of PSCs based on the pristine and modified NiO_x HTLs.

Table 1 Photovoltaic parameters of PSCs based on the pristine and modified NiO_x HTLs

Devices	Best PCE (%)	J_{SC}[a] (mA cm^{-2})	V_{OC}[a] (V)	FF[a] (%)	PCE[a] (%)
Pristine	13.98	20.46	0.97	65.39	12.94
NiO_x/NH_4PF_6	17.28	21.82	1.01	70.97	15.62
$NiO_x/LiPF_6$	14.87	20.99	0.97	68.54	14.03
$NiO_x/NaPF_6$	14.88	20.73	0.99	69.3	14.26

[a] The average photovoltaic parameters were obtained from 30 devices.

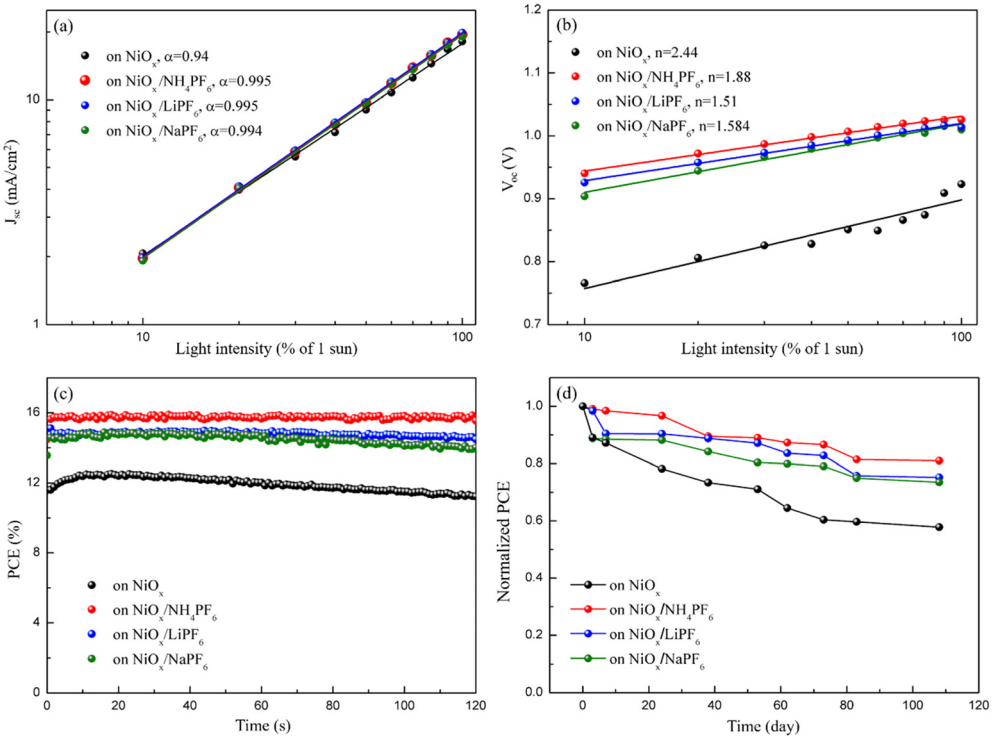

Fig. 8 (a) J_{SC} and (b) V_{OC} values *versus* light intensity, (c) steady-state PCE output at the maximum power point, and (d) stability test of PSCs based on the pristine and modified NiO_x HTLs.

the photo-generated current density, and J_0 is the dark saturation current. As evident in the V_{OC}–light intensity relation, the ideality factor n typically denotes the dominant recombination mechanism in solar cells.[48] The reduction in the n value indicates that the trap-mediated Shockley–Read–Hall (SRH) recombination through interfacial defects is prohibited.[49] The n values of the devices with the NH_4PF_6, $LiPF_6$, and $NaPF_6$-modified HTLs (n = 1.88, 1.51, and 1.584) are smaller than that of the controlled device (n = 2.44), showing effective suppression of the SRH recombination pathway by salt incorporation. Fig. 8c plots the steady-state PCE output at the maximum power point of the corresponding devices before and after salt modification. The PCE of the unmodified device gradually decreased from 12.74% to 11.46% within 120 s, while the three salt-modified devices possessed a stable PCE output, indicative of excellent photostability. To explore the device lifetime of the PSCs, the manufactured PSCs were stored in a humidity control box at room temperature with 40% RH and their device performance was acquired at certain intervals, as shown in Fig. 8d. After 108 days, the PCE of the unmodified device decreased by 42.17% of the initial efficiency; moreover, the PCE of devices modified with NH_4PF_6, $LiPF_6$, and $NaPF_6$ salts was reduced by only 19%, 24%, and 26.5% of the original efficiency, respectively. The improvement in the stability of the PSCs by salt modification can be attributed to the reduction in defect state density and optimized contact at the NiO_x/perovskite interface, as mentioned in the previous section.

4. Conclusions

The three hexafluorophosphate salts were proven to serve as effective interfacial modifiers for NiO_x in reducing defects and enhancing the photovoltaic performance of PSCs. Relative to the unmodified device, the devices based on the salt-modified NiO_x showed markedly enhanced performance. Notably, the utilization of NH_4PF_6-modified

NiO_x yielded optimal results, with a maximum PCE of 17.28% and excellent device lifetime of up to 108 days. The performance enhancement is attributed to advantageous energy level alignment, passivation of interfacial carrier traps, and perovskite grain quality. This work demonstrates not only a simple strategy toward defect passivation in PSCs but also the functionality of the interlayer between NiO_x and the perovskite to improve the device efficiency and stability.

Conflicts of interest

There are no conflicts to declare.

Acknowledgements

The authors thank the National Science and Technology Council of Taiwan under Contract No. MOST 110-2221-E-A49-082-MY3 for financially supporting this work.

References

1 E. D. Gaspera, Y. Peng, Q. Hou, L. Spiccia, U. Bach, J. J. Jasieniak and Y.-B. Cheng, Ultra-thin high efficiency semitransparent perovskite solar cells, *Nano Energy*, 2015, **13**, 249–257.
2 Y. Rong, Y. Hu, A. Mei, H. Tan, M. I. Saidaminov, S. I. Seok, M. D. McGehee, E. H. Sargent and H. Han, Challenges for commercializing perovskite solar cells, *Science*, 2018, **361**, eaat8235.
3 L. Ma, F. Hao, C. C. Stoumpos, B. T. Phelan, M. R. Wasielewski and M. G. Kanatzidis, Carrier Diffusion Lengths of over 500 nm in Lead-Free Perovskite $CH_3NH_3SnI_3$ Films, *J. Am. Chem. Soc.*, 2016, **138**, 14750–14755.
4 M. I. H. Ansari, A. Qurashi and M. K. Nazeeruddin, Frontiers, opportunities, and challenges in perovskite solar cells: A critical review, *J. Photochem. Photobiol., C*, 2018, **35**, 1–24.
5 National Renewable Energy Laboratory (NREL), Best Research-Cell Efficiency chart, **https://www.nrel.gov/pv/cell-efficiency.html**, 2023.
6 J. M. Azpiroz, E. Mosconi, J. Bisquert and F. De Angelis, Defect migration in methylammonium lead iodide and its role in perovskite solar cell operation, *Energy Environ. Sci.*, 2015, **8**(7), 2118–2127.
7 Z. Zheng, S. Wang, Y. Hu, Y. Rong, A. Mei and H. Han, Development of formamidinium lead iodide-based perovskite solar cells: efficiency and stability, *Chem. Sci.*, 2022, **13**, 2167–2183.
8 K. Wang, Z. Jin, L. Liang, H. Bian, D. Bai, H. Wang, J. Zhang, Q. Wang and S. Liu, All-inorganic cesium lead iodide perovskite solar cells with stabilized efficiency beyond 15%, *Nat. Commun.*, 2018, **9**, 4544.
9 T. Singh and T. Miyasaka, Stabilizing the Efficiency Beyond 20% with a Mixed Cation Perovskite Solar Cell Fabricated in Ambient Air under Controlled Humidity, *Adv. Energy Mater.*, 2018, **8**, 1700677.
10 X. Li, J. Yang, Q. Jiang, W. Chu, D. Zhang, Z. Zhou, Y. Ren and J. Xin, Enhanced photovoltaic performance and stability in mixed-cation perovskite solar cells via compositional modulation, *Electrochim. Acta*, 2017, **247**, 460–467.
11 L. Gil-Escrig, C. Momblona, M.-G. La-Placa, P. P. Boix, M. Sessolo and H. J. Bolink, Vacuum Deposited Triple-Cation Mixed-Halide Perovskite Solar Cells, *Adv. Energy Mater.*, 2018, **8**, 1703506.
12 M. Bidikoudi and E. Kymakis, Novel approaches and scalability prospects of copper based hole transporting materials for planar perovskite solar cells, *J. Mater. Chem. C*, 2019, **7**, 13680–13708.
13 L. Xu, X. Chen, J. Jin, W. Liu, B. Dong, X. Bai, H. Song and P. Reiss, Inverted perovskite solar cells employing doped NiO hole transport layers: A review, *Nano Energy*, 2019, **63**, 103860.
14 Y. Bai, S. Xiao, C. Hua, T. Zhang, X. Meng, Q. Li, Y. Yang, K. S. Wong, H. Chen and S. Yang, A pure and stable intermediate phase is key to growing aligned and vertically monolithic perovskite crystals for efficient PIN planar perovskite solar cells with high processibility and stability, *Nano Energy*, 2017, **34**, 58–68.
15 Y. Yao, C. Cheng, C. Zhang, H. Hu, K. Wang and S. De Wolf, Organic Hole-Transport Layers for Efficient, Stable, and Scalable Inverted Perovskite Solar Cells, *Adv. Mater.*, 2022, **34**, 2203794.
16 G. Li, Z. Su, L. Canil, D. Hughes, M. H. Aldamasy, J. Dagar, S. Trofimov, L. Wang, W. Zuo, J. J. Jerónimo-Rendon, M. M. Byranvand, C. Wang, R. Zhu, Z. Zhang, F. Yang, G. Nasti, B. Naydenov, W. C. Tsoi, Z. Li, X. Gao, Z. Wang, Y. Jia, E. Unger, M. Saliba, M. Li and A. Abate, Highly efficient p-i-n perovskite solar cells that endure temperature variations, *Science*, 2023, **379**, 399–403.
17 D. K. Maram, M. Haghighi, O. Shekoofa, H. Habibiyan and H. Ghafoorifard, A modeling study on utilizing ultra-thin inorganic HTLs in inverted p–n homojunction perovskite solar cells, *Sol. Energy*, 2021, **213**, 1–12.
18 Y. Shao, C. Zhang, S. Wang, Y. Yan, Y. Feng, J. Bian and Y. Shi, Insight into the Interfacial Elastic Contact in Stacking Perovskite Solar Cells, *Adv. Mater. Interfaces*, 2019, **6**, 1900157.
19 S. Im, W. Kim, W. Cho, D. Shin, D. H. Chun, R. Rhee, J. K. Kim, Y. Yi, J. H. Park and J. H. Kim, Improved Stability of Interfacial Energy-Level Alignment in Inverted Planar Perovskite Solar Cells, *ACS Appl. Mater. Interfaces*, 2018, **10**, 18964–18973.
20 J. Dong, D. Song, J. Meng, Y. Lu, Y. Li, B. Qiao, S. Zhao and Z. Xu, Interface energy level alignment and improved film quality with a hydrophilic polymer interlayer to improve the device efficiency and stability of all-inorganic halide perovskite light-emitting diodes, *J. Mater. Chem. C*, 2020, **8**, 6743–6748.
21 J. Endres, M. Kulbak, L. Zhao, B. P. Rand, D. Cahen, G. Hodes and A. Kahn, Electronic structure of the $CsPbBr_3$/polytriarylamine (PTAA) system, *J. Appl. Phys.*, 2017, **121**, 035304.

22 S. Sajid, A. M. Elseman, H. Huang, J. Ji, S. Dou, H. Jiang, X. Liu, D. Wei, P. Cui and M. Li, Breakthroughs in NiO_x-HTMs towards stable, low-cost and efficient perovskite solar cells, *Nano Energy*, 2018, **51**, 408–424.

23 J. Zhang, J. Long, Z. Huang, J. Yang, X. Li, R. Dai, W. Sheng, L. Tan and Y. Chen, Obstructing interfacial reaction between NiO_x and perovskite to enable efficient and stable inverted perovskite solar cells, *Chem. Eng. J.*, 2021, **426**, 131357.

24 H. Bian, J. You, C. Xu, X. He, M. Wang, Y. Yao, W. Zeng, P. Guo, H. Zhou, D. Lu, Z. Dai, S. Zhang and Q. Song, Chemically suppressing redox reaction at the NiO_x/perovskite interface in narrow bandgap perovskite solar cells to exceed a power conversion efficiency of 20%, *J. Mater. Chem. A*, 2023, **11**, 205–212.

25 C.-Y. Chang, Y.-W. Wu, S.-H. Yang and I. Abdulhalim, Preparation of Nickel Oxide Nanoflakes for Carrier Extraction and Transport in Perovskite Solar Cells, *Nanomaterials*, 2022, **12**, 3336.

26 T. Hu, H. Hou, J. Peng, Q. Wu, J. He, H. Yu, R. Liu, T. Hou, X. Zhou, M. Zhang, X. Zhang, X. Yang, Y. Sun, X. Li and Y. Bai, 4-tert-butylpyridine induced Ni^{3+}/Ni^{2+} ratio modulation in NiO_x hole transport layer towards efficient and stable inverted perovskite solar cells, *Mater. Today Energy*, 2023, **32**, 101245.

27 F. Jiang, W. C. H. Choy, X. Li, D. Zhang and J. Cheng, Post-treatment-Free Solution-Processed Non-stoichiometric NiO_x Nanoparticles for Efficient Hole-Transport Layers of Organic Optoelectronic Devices, *Adv. Mater.*, 2015, **27**, 2930–2937.

28 X. Deng, L. Lu, H. Li and F. Luo, The adsorption properties of Pb(II) and Cd(II) on functionalized graphene prepared by electrolysis method, *J. Hazard. Mater.*, 2010, **183**, 923–930.

29 S. Xiao, C. Liu, L. Chen, L. Tan and Y. Chen, Liquid-crystalline ionic liquids modified conductive polymers as a transparent electrode for indium-free polymer solar cells, *J. Mater. Chem. A*, 2015, **3**, 22316–22324.

30 F. Zhang, R. Ji, Y. Liu, Z. Li, Z. Liu, S. Lu, Y. Wang, X. Wu, H. Jin and B. Cai, Defect-rich engineering and F dopant Co-modulated NiO hollow dendritic skeleton as a self-supported electrode for high-current density hydrogen evolution reaction, *Chem. Eng. J.*, 2020, **401**, 126037.

31 L. Chen, J. Chang, Y. Zhang, Z. Gao, D. Wu, F. Xu, Y. Guo and K. Jiang, Fluorine anion-enriched nickel hydroxyl oxide as an efficient oxygen evolution reaction electrocatalyst, *Chem. Commun.*, 2019, **55**, 3406–3409.

32 Y.-W. Wu, C.-Y. Chang, F.-B. Chiu and S.-H. Yang, Efficient and stable perovskite solar cells using manganese-doped nickel oxide as the hole transport layer, *RSC Adv.*, 2022, **12**, 22984–22995.

33 F. Cao, F. Cheng, X. Huang, X. Dai, Z. Tang, S. Nie, J. Yin, J. Li, N. Zheng and B. Wu, Synergistic Effect between NiO_x and P3HT Enabling Efficient and Stable Hole Transport Pathways for Regular Perovskite Photovoltaics, *Adv. Funct. Mater.*, 2022, **32**, 2201423.

34 A. Kotta, I. Seo, H.-S. Shin and H.-K. Seo, Room-temperature processed hole-transport layer in flexible inverted perovskite solar cell module, *Chem. Eng. J.*, 2022, **435**, 134805.

35 H. Zhang, J. Cheng, F. Lin, H. He, J. Mao, K. S. Wong, A. K.-Y. Jen and W. C. H. Choy, Pinhole-Free and Surface-Nanostructured NiO_x Film by Room Temperature Solution Process for High-Performance Flexible Perovskite Solar Cells with Good Stability and Reproducibility, *ACS Nano*, 2016, **10**, 1503–1511.

36 Z. Huang, D. Ouyang, R. Ma, W. Wu, V. A. L. Roy and W. C. H. Choy, A General Method: Designing a Hypocrystalline Hydroxide Intermediate to Achieve Ultrasmall and Well-Dispersed Ternary Metal Oxide for Efficient Photovoltaic Devices, *Adv. Funct. Mater.*, 2019, **29**, 1904684.

37 S. Ahmad, R. Ma, J. Zheng, C. K. G. Kwok, Q. Zhou, Z. Ren, J. Kim, X. He, X. Zhang, K. M. Yu and W. C. H. Choy, Suppressing Nickel Oxide/Perovskite Interface Redox Reaction and Defects for Highly Performed and Stable Inverted Perovskite Solar Cells, *Small Methods*, 2022, **6**, 2200787.

38 Z.-W. Gao, Y. Wang, D. Ouyang, H. Liu, Z. Huang, J. Kim and W. C. H. Choy, Triple Interface Passivation Strategy-Enabled Efficient and Stable Inverted Perovskite Solar Cells, *Small Methods*, 2020, **4**, 2000478.

39 H. Yi, D. Wang, M. A. Mahmud, F. Haque, M. B. Upama, C. Xu, L. Duan and A. Uddin, Bilayer SnO_2 as Electron Transport Layer for Highly Efficient Perovskite Solar Cells, *ACS Appl. Energy Mater.*, 2018, **1**, 6027–6039.

40 M.-H. Yu, P.-C. Han, C.-C. Lee, I.-C. Ni, Z. Zhu, E. Z. Kurmaev, S. Furukawa, K. C.-W. Wu and C.-C. Chueh, A self-arranged metal–organic polyhedron/fullerene asymmetric structure improves the performance of inverted perovskite solar cells, *J. Mater. Chem. C*, 2022, **10**, 14542–14548.

41 B. Cao, L. Yang, S. Jiang, H. Lin, N. Wang and X. Li, Flexible quintuple cation perovskite solar cells with high efficiency, *J. Mater. Chem. A*, 2019, **7**, 4960–4970.

42 H. Zhang, X. Ren, X. Chen, J. Mao, J. Cheng, Y. Zhao, Y. Liu, J. Milic, W.-J. Yin, M. Grätzel and W. C. H. Choy, Improving the stability and performance of perovskite solar cells via off-the-shelf post-device-ligand treatment, *Energy Environ. Sci.*, 2018, **11**, 2253–2262.

43 S. Ahmad, M. Guan, J. Kim, X. He, Z. Ren, H. Zhang, H. Su and W. C. H. Choy, High-Quality Pure-Phase MA-Free Formamdinium Dion-Jacobson 2D Perovskites for Stable Unencapsulated Photovoltaics, *Adv. Energy Mater.*, 2024, **14**, 2302774.

44 W. Yan, Y. Li, Y. Li, S. Ye, Z. Liu, S. Wang, Z. Bian and C. Huang, Stable high-performance hybrid perovskite solar cells with ultrathin polythiophene as hole-transporting layer, *Nano Res.*, 2015, **8**, 2474–2480.

45 H. Yang, J. Zhang, C. Zhang, J. Chang, Z. Lin, D. Chen, X. Sun, H. Xi, G. Han and Y. Hao, Effect of polyelectrolyte interlayer on efficiency and stability of p-i-n perovskite solar cells, *Sol. Energy*, 2016, **139**, 190–198.

46 D. Xu, J. Wang, Y. Duan, S. Yang, H. Zou, L. Yang, N. Zhang, H. Zhou, X. Lei, M. Wu, S. Liu and Z. Liu, Highly-Stable $CsPbI_3$ Perovskite Solar Cells with an Efficiency of 21.11% via Fluorinated 4-amino-benzoate Cesium Bifacial Passivation, *Adv. Funct. Mater.*, 2023, **33**, 2304237.

47 T. Wang, H.-L. Loi, J. Cao, Z. Qin, Z. Guan, Y. Xu, H. Cheng, M. G. Li, C.-S. Lee, X. Lu and F. Yan, High Open Circuit Voltage over 1 V Achieved in Tin-based Perovskite Solar Cells with a 2D/3D Vertical Heterojunction, *Adv. Sci.*, 2022, **9**, 2200242.

48 T. Hu, F. Zhang, H. Yu, M. Zhang, Y. Yu, W. Zhang, R. Liu, L. Tian and Z. Ma, Efficient carrier transport via dual-function interfacial engineering using cesium iodide for high-performance perovskite solar cells based on NiO_x Hole transporting materials, *Nano Res.*, 2021, **14**, 3864–3872.

49 P. Caprioglio, C. M. Wolff, O. J. Sandberg, A. Armin, B. Rech, S. Albrecht, D. Neher and M. Stolterfoht, On the Origin of the Ideality Factor in Perovskite Solar Cells, *Adv. Energy Mater.*, 2020, **10**, 2000502.